Chapter 7

Brightness variations

7.1 Foreword

The Io footprint is made of distinct spots (at least three) followed by a downstream tail. In the previous chapters, we analyzed their position, their relative motion, their altitude, their respective sizes, etc.. All these quantities define the spatial characteristic of the phenomenon and were based either on the localization of the features or on the measurement of their extent. It is now time to focus on the second type of information contained in an image: the brightness.

The present chapter is divided into two parts. In the first part, we will mainly focus on short-timescale relative variations of this brightness. Indeed, the Io footprint fluctuates with several different timescales, and each of them is typical of one or several processes. Analyzing these characteristic periods can thus help us in identifying the different ongoing processes.

Moreover, we are also interested into the absolute values of the emitted brightness and power. This information is essential to understand the energies at play both in the whole interaction and in its different parts. Nevertheless, we will see that converting the number of counts accumulated in the detector pixels to a meaningful information is not as easy as it might seem at first sight. First, it is necessary to correctly identify which feature is measured. For example, does the measured power encompass all the spots or just isolate one? On which basis is the mean brightness computed? Second, the observing geometry has to be well understood. Hence, the brightness of a three dimensional optically thin emission region strongly depends both on the observer's position and on the size of the source region, since the light will not accumulate in the same way along the line of sight. As a consequence, new

measurement methods had to be developed based on the accurate estimate of the position and the size of the different footprint features, which is the reason why this chapter comes at the end. All the issues related to the observation geometry which need to be addressed are now discussed in detail.

7.2 Short timescale brightness variations

7.2.1 Publication: *The ultraviolet Io footprint short timescale dynamics*

B. Bonfond, J.-C. Gérard, D. Grodent

Laboratoire de Physique Atmosphérique et Planétaire Université de Liège, Belgium

J. Saur

Institut für Geophysik und Meteorologie Universität zu Köln, Germany

This article was originally published in the March 2007 issue of Geophysical Research Letters (*Bonfond et al.*, 2007).

7.2.1.1 Abstract

The electromagnetic interaction between Io and Jupiter's magnetic field leads to single or multiple ultraviolet spots near the feet of the Io flux tube. Variations of spot numbers and brightness and of inter-spot distances have been observed to be linked to Io's position in its plasma torus. We have studied the evolution of the Io UV footprints with a time resolution of a few tens of seconds using the Space Telescope Imaging Spectrograph (STIS) in time-tag mode. We present evidence of systematic strong brightness variations of the main spots (up to 50%) with a typical growth time of 1 minute. Additionally, unanticipated simultaneous fluctuations of both primary and secondary spots have also been found in the southern hemisphere. Our findings suggest that the footprint brightness is not only actively controlled by the plasma directly interacting with Io but also by the poorly constrained electron acceleration region between Io and Jupiter.

7.2.1.2 Introduction

The presence of ultraviolet (UV) footprints shifted up to 15° downstream from the estimated location of the extremities of the field lines passing through Io (*Clarke et al.*, 1998) is a spectacular signature of the interaction between a satellite and its planet. These features provide an outstanding possibility to remotely sense Io's interaction with Jupiter's magnetosphere. Io's interaction is created by the motion of Io relative to the Io plasma torus (see reviews in *Saur et al.*, 2004 and *Thomas et al.*, 2004), which perturbs the plasma and the magnetic field around Io, and which is also the root cause for the Io footprints (IFP). The first model for Io's interaction, the unipolar-inductor model, was developed before the plasma torus was discovered. In this description, a steady state current loop is formed which connects Io with Jupiter's ionosphere along its magnetospheric field. (e.g. *Goldreich and Lynden-Bell*, 1969). Although Alfvén waves have been considered early for Io's interaction (*Goldreich and Lynden-Bell*, 1969; *Goertz and Deift*, 1973), their importance was firmly established only after the discovery of the dense Io plasma torus by Voyager (*Neubauer*, 1980; *Goertz*, 1980). In this framework, Alfvén waves propagate the perturbations caused by Io towards Jupiter and form an Alfvén wing system, which is inclined with respect to Jupiter's magnetic field in the downstream direction. Later models (e.g. *Wright and Schwartz*, 1989) predict substantial reflections of the Alfvén waves at the torus boundaries. Furthermore, models considering the electron finite inertia (*Crary*, 1997) imply the generation of electron beams towards Jupiter. Analysis of Galileo observations (*Chust et al.*, 2005) suggests that the low frequency Alfvén waves should be reflected while high frequency, small scale waves are able to cross the torus boundaries. Io's interaction also generates a wake of slow plasma behind Io. The eventual acceleration of the wake particles through momentum transfer from the Jovian ionosphere drives an electric current along the field lines (*Hill and Vasyliūnas*, 2002; *Delamere et al.*, 2003) that causes the trailing tail observed downstream of the footprints on ultraviolet and infrared images (e.g. *Clarke et al.*, 2002; *Connerney and Satoh*, 2000). Observations of the IFP demonstrate that Io's interaction leads to acceleration and precipitation of ∼50 keV electrons in the Jovian ionosphere (*Gérard et al.*, 2002). The collision of these particles withH_2 molecules and H atoms causes optical emissions at both UV and IR wavelengths. The primary spot is frequently followed downstream by one or several secondary spots (*Clarke et al.*, 2002; *Connerney and Satoh*, 2000). Their location and the inter-spot distances appear to be consistent with Alfvén wave reflections

inside the torus (*Gérard et al.*, 2006). The interaction between the plasma torus and Io's ionosphere also gives rise to auroral emissions at Io. Auroral emission is observed within Io's atmosphere on the sub-Jovian and the anti-Jovian sides of Io (*Roesler et al.*, 1999; *Oliversen et al.*, 2001). The authors show that the intensity of this emission includes temporal variability on time scales of ca. 15 min. The present study focuses on the footprint UV emissions and their fluctuations. An increase of the footprint brightness has been found when Io is near the center of the torus, where the plasma is denser (*Gérard et al.*, 2006). This result suggests that the IFP long timescale brightness variations are controlled by the strength of the Io-plasma torus interaction. In situ measurements (*Frank and Paterson*, 2000a) and Io auroral observations (*Roesler et al.*, 1999; *Oliversen et al.*, 2001) have shown that the interaction between Io and the plasma torus contains a fastly varying component, but no counterpart has been observed so far for the footprint. Here we present evidence that the IFP is also a highly dynamic process on timescales around one minute.

7.2.1.3 Data processing

Most of the previous work on the Io UV footprints used time integrated images provided by the successive cameras (e.g. FOC, WFPC2, STIS and ACS) on board the Hubble Space Telescope (HST). During the five Jovian auroral observation programs conducted with the HST/STIS camera throughout its lifetime (from 1997 to 2004), 43 imaging observations (31 in the northern hemisphere and 12 in the southern one) were obtained in time-tag mode. In this observation mode, the positions and the arrival time of the incoming photons are registered. This specific capability of the Multi-Anode Microchannel Array (MAMA) photon counting technology has a time resolution of 125 µs. Each pixel of the 1024×1024 pixel detector subtends a 0.024 arcsec angle and the point spread function covers approximately a 3×3 pixels square. All the observations considered in this study were made with the SrF2 filter (central wavelength: 148 nm, FWHM: 28 nm) which rejects most of the Ly-α emission, largely contaminated by the geocoronal dayglow emissions. The duration of the time-tag sequences varied from 120 to 300 seconds. Most include one or two event stream interruptions due to buffer overflows. The collections of photon detection events are used to reconstruct images which may be integrated over any chosen exposure time by selecting the events in the required time range. In order to achieve an adequate balance between time-resolution and signal-to-noise

ratio, we build 10-second exposure images from the time-tag datasets. The resulting sequences of images were then processed as standard STIS images, that is, dark count, flat field and geometric corrections have been performed. All time-tag observations considered here focus on the auroral morphology, but not specifically on Io footprints. Therefore, the Io footprint is not always visible nor in a favorable position. As a result, only 12 sequences in the north and 5 in the south turned out to be suitable. The Io longitudes coverage (System III) corresponding to the northern footprint observations ranges from 123° to 201° while the southern one spans 84° to 99°. In order to compensate for the footprint motion during the exposure, the sub-images were shifted according to the deviation deduced from the VIP4 magnetic field model (*Connerney et al.*, 1998). This technique allows one to stack the footprint sub-images from the same sequence in the same reference frame. We then subtracted the Jovian background emissions in order to isolate the intrinsic IFP emissions. The footprint emission brightness as a function of longitude was obtained by extracting a 21-pixel wide stripe containing the main spots and the beginning of the tail. The brightnesses were integrated over the 21 pixels in order to obtain a linear profile. Figure 7.1 presents an example of a linear profile and its characteristic behavior during a time-tag sequence. Using the correction deduced from the VIP4 model, all the profiles can be plotted in the same reference frame with the x-axis for the longitudes and the y-axis for time to visualize the temporal evolution of the footprints. Figure 7.2 shows examples of the typical behavior of aligned and color-coded profiles both for the northern and the southern hemispheres. That way, successive profiles can be summed in order to integrate the brightness over a longer time period, and therefore to increase the signal-to-noise ratio. In Figure 7.2, a temporal smoothing of the profiles has been performed since all the lines represent profiles with a 20-second integration time, even if the time step between two lines is 10 seconds. The vertical alignment of the brightness peaks of the profiles in this figure confirms that the VIP4 accuracy is sufficient for lining-up the profiles.

7.2.1.4 Observations

Brightness fluctuations In the northern footprint brightness profiles (e.g. Figure 7.1), the main spot can always be clearly distinguished from the secondary ones and from the trailing tail. The second spot is usually fainter and can hardly be identified in short exposures (∼10s) but it is revealed by increasing the integration time. Significant brightness variations of the main spot are systematically observed

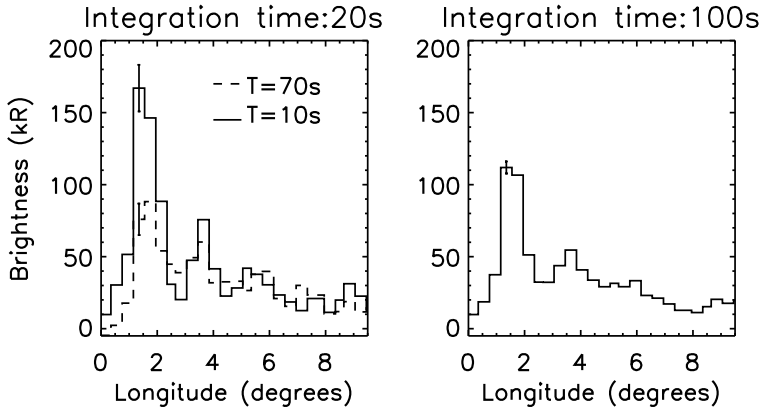

Figure 7.1: (Left) Profiles of the northern footprint integrated over 20 seconds. The first exposure starts 10 seconds after the beginning of the time-tag sequence while the second one starts 60 seconds later. This typical time-tag sequence shows significant brightness variations of the main footprint. (Right) Profile of the same northern footprint integrated over 100 seconds. The weak secondary footprint barely identifiable on 20-second exposures is now clearly distinguished. The sequence was observed the 26 February 2000 at 01:57:41 UT.

in all northern hemisphere datasets, ranging from 17% to 50%. Figure 7.3 demonstrates that these fluctuations are far above the noise level and independent from background fluctuations. Moreover, a characteristic growth time of ∼60 seconds can be determined from the light curves (Figure 7.4a). No System III influence of the short timescale brightness variability has been identified, although the limited number of sequences does not permit any definitive conclusion. In the southern hemisphere, when a secondary spot is present, it is generally as bright or brighter than the primary spot, so that both spots can be clearly identified in the profiles. In all southern sequences, the brightness variations are on the same order of magnitude as in the north. The variations range from 25% to 36% for the primary spot and from 20% to 32% for the secondary spot.

Simultaneous fluctuations In the southern hemisphere, the correlation between the brightness of the first two spots is striking (see for example Figure 7.4b and 7.4c). In the present dataset, the secondary spot is separated from the first one in four out of five cases. In three cases out of four, the correlation coefficients for the temporal evolution of the intensities of the primary and the secondary spot calculated for the sequences preceding the data interruptions is as high as 0.9, largely above the significance threshold (∼0.7 at 99%). In the fourth case, no correlation is observed.

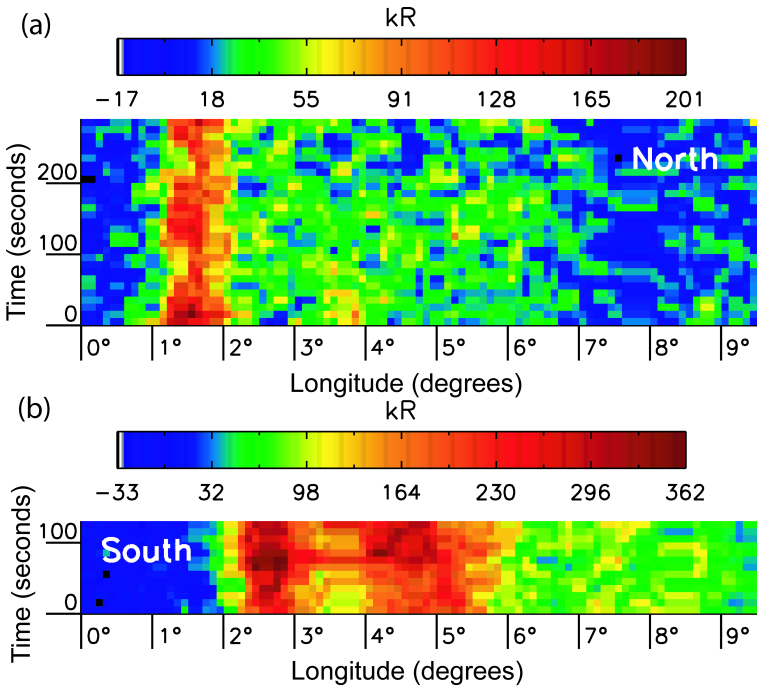

Figure 7.2: (a) Evolution of the profiles of the same northern footprint as in Figure 7.1. The horizontal axis represents the longitude (one mark is equivalent to 1°) and the vertical axis represents the time (one mark corresponds to 100 seconds). Each line is a color-coded profile with a 20 seconds exposure time. (b) Evolution of the profiles of the southern footprint sequence observed the 8 August 1999 at 12:56:47 UT. Both main and secondary footprints brightnesses increase simultaneously.

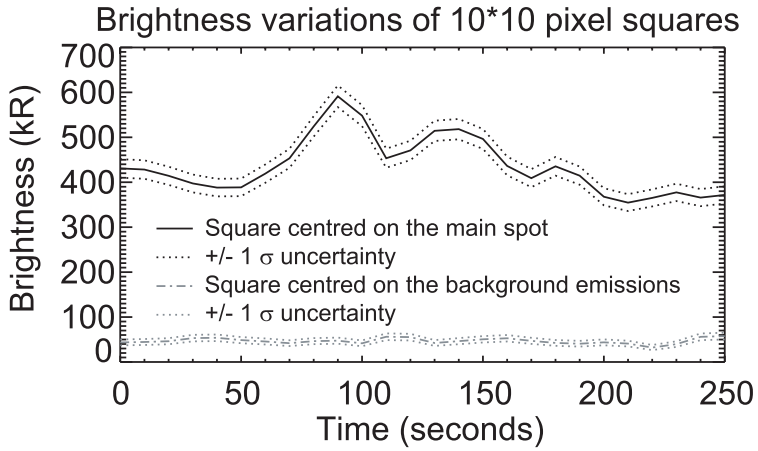

Figure 7.3: Light curves of 10×10-pixel squares centered respectively on the main spot and on the background Jovian emissions close to the footprint. The IFP brightness fluctuations are clearly statistically significant and independent from background variations. This northern footprint sequence was observed the 16 December 2000 at 11:25:51 UT.

These three cases occurred when Io was located in the same range of longitudes (i.e. between 84° and 99°). In this sector, Io is southward from the centrifugal equator of the torus (i.e. centrifugal latitudes between –1.2° and –2.9°), but still in its central region. Figures 4b and 4c show two examples of light curves of both primary and secondary southern spots. These plots suggest that in the first case, the variations of the second spot lag by ∼10 seconds the variations of the first one, while in the other case the secondary spot maximum precedes the primary one. Nevertheless, considering the brightness inaccuracies and the 10 seconds time step of the samples, this slight shift of the light curves is possibly not significant.

7.2.1.5 Discussion

We found significant footprint brightness variations for all observed sequences (i.e. both North and South), even though they were acquired at different times between 1999 and 2003. This provides strong evidence that the Io controlled auroral emissions are not in a steady state but highly dynamic. This variability may be attributed to intrinsic inhomogeneities of the interacting media (i.e. Io's ionosphere, the plasma torus, the Jovian ionosphere, etc.) or to non-linearities occurring during the propagation of the perturbation (i.e. wave breaking, phase mixing, etc.). *Roesler et al.* (1999) have observed fluctuations of the auroral emissions on Io with a timescale

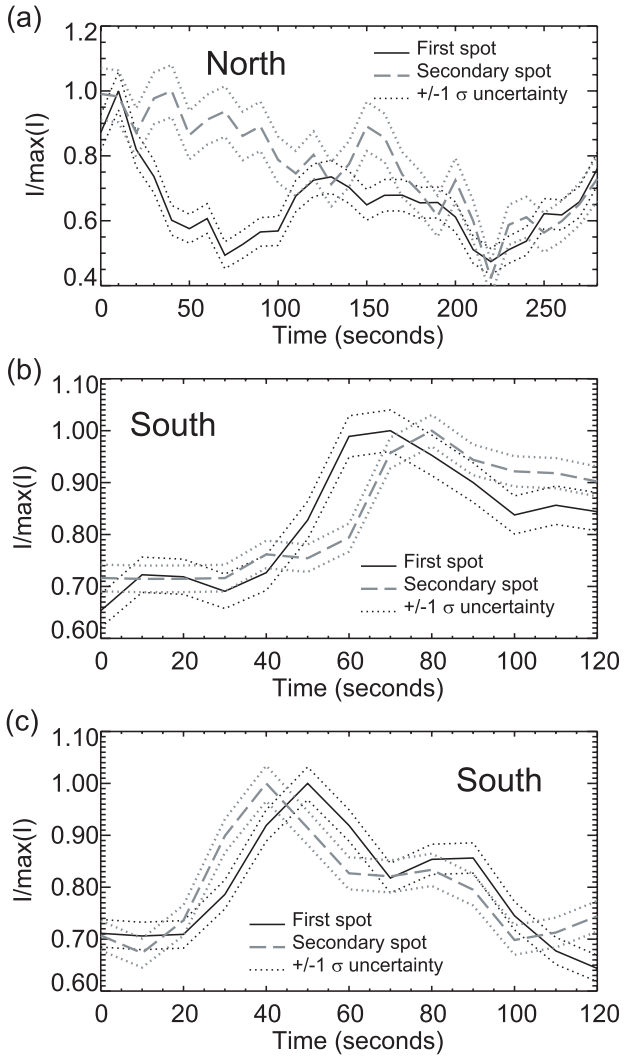

Figure 7.4: (a) Temporal evolution of the relative brightness of the first and the secondary spots in the profiles showed in Figure 1. The fluctuations of the first spot have a typical growth time of ~1 minute. Variations of the faint secondary spot are also present, but are not correlated to those of the main spot. (b) Temporal evolution of the relative brightness of the first and the secondary spots of a southern footprint. The sequence was observed the 8 August 1999 at 12:56:47 UT. On these light curves, the significant variations of both spots are clearly correlated. (c) Second example of time evolution of the relative brightness of the first and the secondary spots of a southern footprint observed the 12 August 2000 at 09:15:18 UT.

of 15 minutes and ascribed them to large-scale local variations in the plasma torus, while *Oliversen et al.* (2001) more precisely attributed them to electron energy flux variations in the torus. These fluctuations are one order of magnitude longer than those observed in our time-tag data. However, given the weakness of the auroral emissions on Io, the short timescale variations described here would remain indistinguishable in the auroral data for Io. Io related decametric radio emissions also show a short timescale component (S-bursts) occurring between Jupiter's surface and 0.4 Jovian radius (e.g. *Ergun et al.*, 2006). However, the time scales (from 0.25 second to 0.025 second) as well as the electron energies involved ($\sim$4 keV with 1 keV potential jumps) (*Hess et al.*, 2007) can hardly be linked to the timescales ($\sim$1 min) and the energies ($\sim$50 keV) discussed here. The simultaneous variations of the southern spots are even more intriguing. Indeed, if the brightness variations are due to a temporally varying strength of the interaction generated at Io, a delay between the primary and the secondary brightness peaks is expected. In the Alfvén wing theory, the very occurrence of the secondary spot is due to this delay, as the consequence of the longer path of the reflected perturbation. If one considers reflections inside the torus and given the Alfvén speed in the dense torus, the delay would be on the order of 13 minutes (*Crary and Bagenal*, 1997). If reflections occur between the Jovian ionosphere and the outer edge of the torus, the associated delay would remain between 30 and 90 seconds. Moreover, the calculated inter-spot distance would lie between 0.14° and 0.7° and would be independent of Io's position in the torus, in contrast with the observations. As a consequence, even if localized fluctuations of the initial Io-plasma torus interaction may partly explain the footprint brightness variability, they provide no explanation for the simultaneous fluctuations of the southern spots. This result might imply that the acceleration mechanism leading to the electron precipitation also experiences short timescale variations. At Earth, flickering auroras are very localized spots whose brightness is probably modulated by plasma wave induced processes also occurring in the acceleration region (e.g. *Sakanoi et al.*, 2005). Pulsating auroras are another type of fastly-varying auroral phenomenon at Earth. They appear to involve oscillations between auroral precipitation and generation of whistler waves in the equatorial plane (e.g. *Nemzek et al.*, 1995).

7.2.1.6 Conclusions

This study has unveiled a previously unexplored aspect of the Io footprint auroral emissions: their short timescale (∼1 minute) dynamics. Additionally, quasi-simultaneous and highly correlated variations of primary and secondary footprint brightness suggest that the modulation is not only driven by the Io-plasma torus interaction as suggested by the long timescale brightness variations, but also by the acceleration process occurring between the torus and Jupiter. Since the acceleration mechanism is still poorly understood because of the lack of observational constraints, the amplitude of the brightness variations as well as their characteristic lengths provide essential characteristics for building future quantitative models.

7.3 Epilogue

During the 10862 large HST observation program, several orbits have been specifically dedicated to the Io footprint. The exposure time of these images has been reduced to 30 seconds, with an image acquired every ∼70 seconds. This sampling rate does not allow one to track the brightness variations with as much accuract as for time-tag sequences, even though brightness variations of similar scale have been found (Figure 7.5).

Subsequent observations confirmed the significance of the study of the short timescale variations of the footprint brightness. First, *Grodent et al.* (2009) found similar brightness variations for the Ganymede footprint. Based on seven STIS time-tag sequences, these authors showed that the GFP power experiences quasi-periodic variations (Figure 7.6 a and b) or more chaotic behaviors (7.6 c), but with similar timescales. They proposed two possible mechanisms for these variations. These variations could be related to bursty reconnection events which are expected to occur on timescales of several tens of seconds. As a matter of fact, MHD simulation by *Jia et al.* (2009b) indicate that Ganymede's magnetopause could oscillate with such timescales, which appears to be consistent with in-situ Galileo magnetic field observations. On the other hand, quasi-periods of 100 seconds could also be a typical timescale for the generation of double layers in the Jovian ionosphere when subject to strong electric currents. Indeed, the second type of Io related observations with similar timescale has been reported by *Hess et al.* (2009), based on the analysis of S-burst radio emissions revealing vertically drifting acceleration structures with a re-

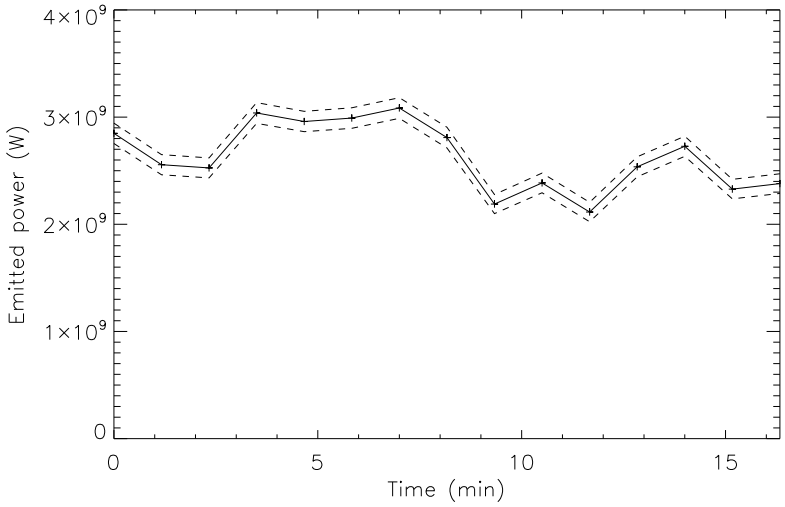

Figure 7.5: Variations of the MAW spot emitted power in the southern hemisphere in the Io System III longitude range between 12° and 20°. The variations are on the order of 37% of the mean power.

appearance quasi-period of 200 seconds. These variable acceleration structures are probably not the main cause for the electron acceleration but can possibly provide additional energy and trigger the fast brightness fluctuations. The interpretation of the 100 second timescale as a typical timescale of the Jovian ionosphere offers the advantage to explain both the Io and Ganymede footprint variations with a single mechanism.

7.4 System III related brightness variations

7.4.1 Introduction

7.4.1.1 Possible scenarios for System III related brightness variations

While the short timescale variability of the IFP spots was relatively unexpected, a correlation of the brightness with the System III location, i.e. a variability on timescales of several hours (one Io revolution in System III lasts for ∼13 hours), is less surprising. Several scenarii relating both quantities can be viewed. *Serio and Clarke* (2008) considered three of them:

1. Collisional interaction at Io: if the strength of the interaction at Io controls the intensity of the Alfvén waves and if intermediate processes do not cause further modulation of the brightness, the evolution of the brightness should be the same in both hemispheres and peak when Io is near the dense torus center.

2. Poynting flux loss: this scenario puts the emphasis on the possible Poynting flux loss when the Alfvén waves travel into the plasma torus. When Io is in the northern part of the torus, the waves traveling towards the north pole can fastly escape the torus while waves going towards the south have to cross the entire torus and weaken and vice-versa when Io is in the southern part of the torus. As a consequence, the northern main spot would be the brightest at 200° System III longitude and the weakest around 20°. The southern footprint would exactly follow the opposite behavior.

3. Pitch-angle diffusion aurora: if the incoming electrons have a given pitch angle distribution, the maximum brightness will occur when the loss cone is maximum, i.e. when the magnetic field strength is minimum in the Jovian ionosphere.

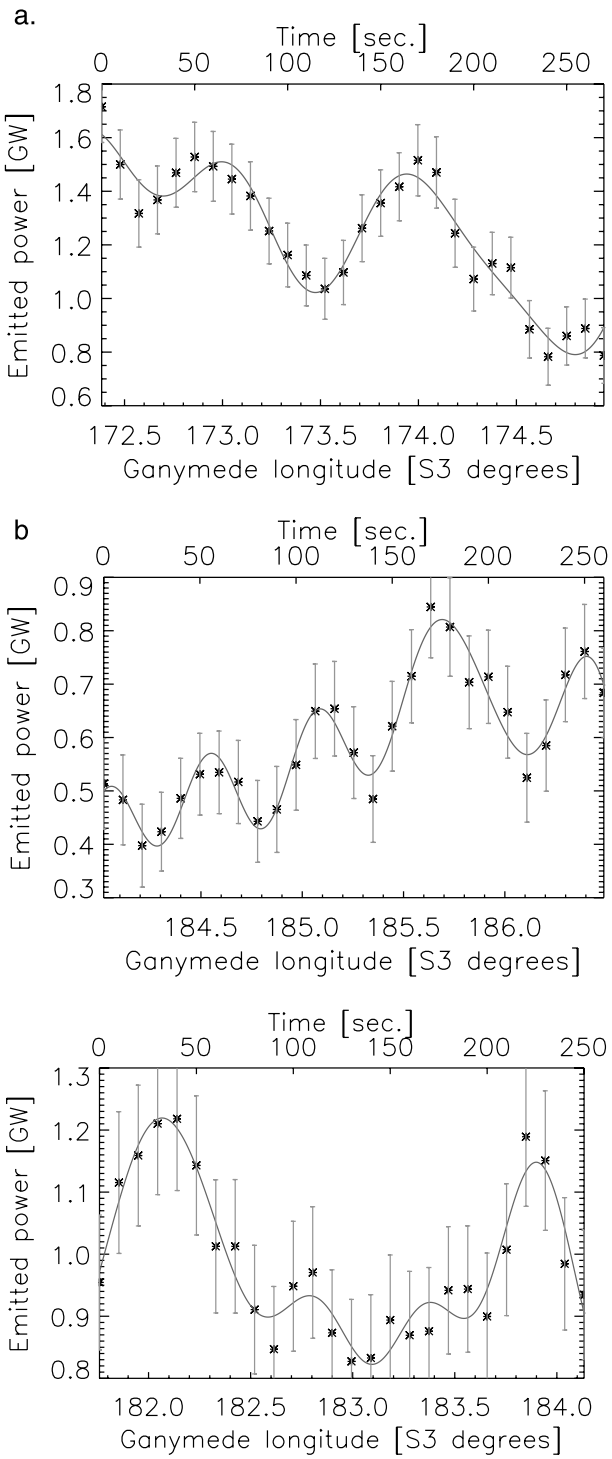

Figure 7.6: Short timescale variations of the Ganymede footprint brightness. In panels a) and b), quasi-periodic variations of the emitted power can be seen while variations shown in panel c) are irregular, but the growth time remains similar (from *Grodent et al.*, 2009).

A fourth scenario was foreseen by *Connerney et al.* (1993) with consequences similar to the third scenario. If the Jovian ionospheric Pedersen conductivity is the main parameter controlling the current intensity and if the precipitation flux is correlated with this current, the maximum brightness should be found when the conductivity is maximum. Since the Pedersen conductivity is approximately inversely proportional to magnetic field strength, the brightest spots should be seen when the surface magnetic field intensity is minimum. A fifth reason to anticipate an increase of the MAW spot maximum brightness is the motion of the TEB spot relative to it. When Io is near the torus center, the two spots merge together and the resulting spot should be as bright as the sum of their individual brightness. It is noteworthy that this scenario has broadly similar consequences as the first one. It should also be noted that these scenarii do not necessarily exclude each other and thus a combination of these effects could also be expected.

We showed in the previous chapters that the different spots have different origins and their response to the various relevant parameters could also change from one spot to another. The MAW spot is expected to be the consequence of the direct electron acceleration at the foot of the direct Alfvén wing. On the other hand and according to our interpretation, the TEB spot is caused by the anti-planet-ward acceleration of trans-hemispheric electron beams. Since it is caused by electrons accelerated in one hemisphere and precipitated into the other, the TEB spot brightness could be more sensitive to the asymmetry between the northern and southern magnetic field strength than the other two. Another possible reason that would justify a different behavior for the different spots could be that the RAW spot is the most sensitive to the Poynting flux loss because of the larger path length.

7.4.1.2 Previous studies

The Io footprint brightness in the FUV domain ranges between 25 and 700 kR (see Table 1.1). In the present section, we will only recall the studies that specifically studied the variations of the brightness as a function of the Io longitude. *Connerney et al.* (1993) suggested that the apparent lack of detection of the infrared northern IFP in the 90°-240° System III longitude range could be related to the expected high surface magnetic field strength in this region. Later observations acquired in the FUV domain with the WFPC2 camera infirmed this absence of detection, since several occurrences of northern footprints were seen in this longitude range (*Clarke et al.*, 1998). However, despite the noticeable scatter of the data points, they did not

find any trend between the IFP brightness and Io's longitude, most probably because of the large error bars related to the WFPC2 low sensitivity. The first conclusive relationship between the brightness and the Io location was reported by *Gérard et al.* (2006), based on STIS observations acquired between December 2000 and February 2003. They showed that the maximum IFP brightness increases when Io's centrifugal latitude decreases (Figure 1.11). They also applied a correction assuming a plane parallel atmosphere to take the limb brightening effect into account. The authors attributed the increase of the IFP brightness as Io settles into the dense torus center to the expected enhancement of the Io-magnetosphere interaction. Finally, *Serio and Clarke* (2008) studied the evolution of the footprint brightness on STIS images acquired from August 1999 to January 2001. They tested the variation of the brightness against the three scenarii mentioned above and concluded, like *Gérard et al.* (2006), that the strength of the interaction is the main driver for the mean IFP brightness.

7.4.2 How to estimate the brightness?

Most studies discussing the intensity of the auroral features express the brightness in Rayleighs or in kilo-Rayleighs. However, the Rayleigh (R) is a very peculiar unit that should be handled with care. This radiance unit "measures the absolute angular surface brightness of spatially extended light emitting sources" (*Baker*, 1974). 1kR represents 10^9 photons $m^{-2}s^{-1}$ within 4π steradians. This unit was initially used for airglow emissions on Earth. It is also very convenient to use in the case of auroral emission because its measurement summarizes the light emission in the air column. Consequently, it can be related to the precipitated energy flux through the use of appropriate energy degradation models (*Gérard and Singh*, 1982).

An important issue when providing brightnesses in Rayleigh is the spectrum of emission source and the instrumental throughput effects. The number of counts/s measured on different images acquired with different filters varies with the throughput of these filters. Nevertheless, we would like to be able to compare images acquired with a filter rejecting the Lyman-α with images including these emissions. The idea is to multiply a synthetic H_2 and H FUV auroral spectrum attenuated below $\sim$130 nm by a factor of 0.4[1] with the suitable instrumental throughput to compute the ratio between the number of originally emitted photons and the number of

[1]This level of methane absorption corresponds to a color ratio of 2.5.

	brightness	power
CLEAR	667.56	$\frac{d^2}{7.5161\times10^9}$
F25SRF2	1975.5	$\frac{d^2}{2.5397\times10^9}$
F115LP	328.06	$\frac{d^2}{1.0024\times10^{10}}$
F125LP	468.21	$\frac{d^2}{7.0234\times10^9}$

Table 7.1: Conversion coefficients from counts per second to kilo-Rayleighs and Giga-Watts. d represents the Earth-Jupiter distance in km. For the two ACS filters, i.e. the F115LP filter and the F125LP filter, these coefficients should be applied after the 1.63 coefficient correction described in Section 2.5.2.

actually received photons (*Grodent et al.*, 2003a). Assuming all auroral emissions have approximately the same FUV spectrum, we can then convert count rates into emitted radiance (see Table 7.1). It should be nevertheless noted that a corollary to this process is that the conversion coefficients from counts per second to kilo-Rayleigh are only appropriate for H_2 and H auroral emissions. Studies focusing on the reflected sunlight for example should consider another conversion coefficient based on its specific spectrum. In conclusion, when we provide numbers in kilo-Rayleighs, we should always specify the emitting source under consideration.

Another key issue is the limb brightening. When analyzing HST images of giant planet aurorae, emissions appearing close to the limb always look brighter than those appearing closer to the planetary center. This limb brightening is caused by the geometrical accumulation of optically thin emissions along the line of sight. Since this effect can increase the observed brightness by a factor of 10 (*Grodent et al.*, 1997), previous works made use of different strategies to circumvent this issue. In order to compare images with different observation geometries *Clarke et al.* (1998) applied the plane parallel correction[2] to convert the apparent brightness to the brightness that would be expected if the IFP was located on the central meridian at 67° latitude. *Gérard et al.* (2006) divided the observed brightness by the cosine of the zenith angle, implicitly assuming an extended plane parallel emitting layer as well. Contrary to *Clarke et al.* (1998), they provided a corrected value for an observer looking at nadir. Alternatively, *Serio and Clarke* (2008) do not provide a description of their correction method, but the fact that their correction

[2]The plane parallel correction assumes that the atmosphere can be modeled as a flat emitting layer. If α is the zenithal angle, i.e. the angle between the observer and the normal to the plane, than the correction coefficient to convert the observed brightness into the brightness that an observer looking at the nadir would see is simply $1/\cos(\alpha)$.

only depends on the distance to the limb suggests that it relies on the assumption of an extended emitting shell. Indeed, we managed to reproduce fairly well their optical depth correction factor by means of a spherical shell with an exponential vertical profile (Figure 7.7). In this figure, the vertical dash-dotted line represents the minimum distance to the limb under which *Serio and Clarke* (2008) consider their correction to become unreliable. We note that above this value, differences with the plane parallel correction are barely noticeable. Finally, their corrected value assumes a footprint located on the central meridian at 67° latitude like in *Clarke et al.* (1998).

The two above methods assume that the horizontal extent of the IFP is large. As detailed in Chapter 6, this assumption is not justified since images of the IFP when observed from the side demonstrate that the IFP is a thin curtain not broader than 200 km. Figure 7.8 shows simulated images of the hypothetical footprints made of a single spot (900×200 FWHM) followed by an extended tail (e-folding distance: 20000 km). Their spatial extent is exactly the same on every image, but the contour along with they are set is (from left to right) the equator, the 50th parallel and the 80th parallel respectively. We note that the maximum brightness decreases as the spot approaches the limb, which is the opposite behavior than expected from limb brightening from an extended area. Nevertheless, tail emissions on the right-hand image shows that some limb brightening actually takes place and increases the apparent brightness in some places. In conclusion, no simple correction can be applied to deduce the vertical brightness from the apparent one. All the complexity of the observing geometry has to be accounted for to retrieve information on the precipitated energy fluxes. As a result, we propose a new method to estimate the vertical brightness of the IFP spots and tail. It consists in comparing the emissions observed with the HST STIS and ACS instruments with realistic simulations of the emission regions.

7.4.3 Emission model

The purpose of our emission model is to reproduce as accurately as possible the shape and brightness of the different constituents of the Io footprint in order to compare model images to the actual planetary disk subtracted images. For each HST image, four model images are computed. One for each of the three spots and one for tail. Each sub-image is built such that the maximum brightness as seen from

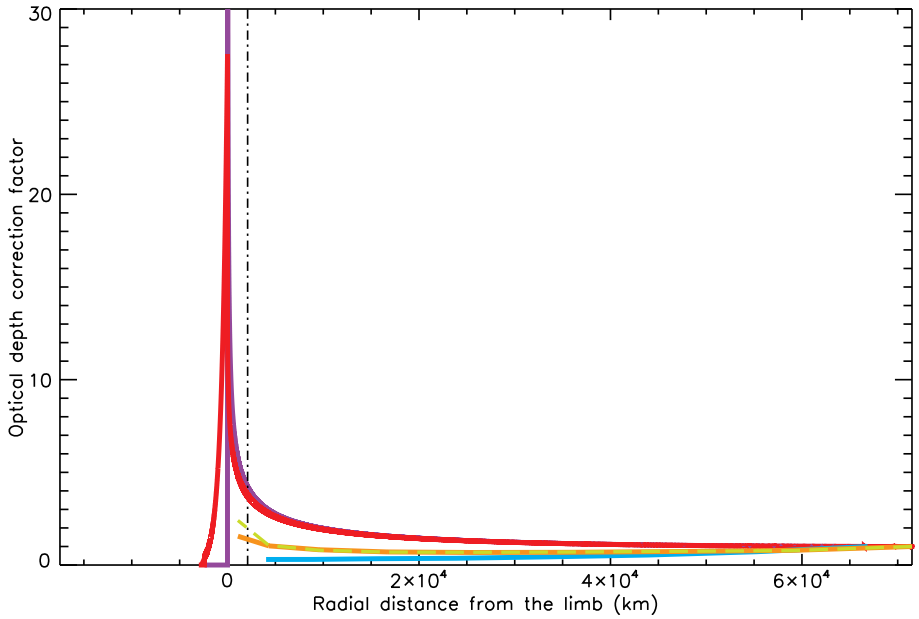

Figure 7.7: Evolution of the optical depth correction factor as a function of the radial distance from the limb. The purple line stands for the $1/\cos(\alpha)$ correction (with α being the zenith angle). The red line represents the spherical shell correction assuming an exponential vertical profile (scale height: 600 km). The cyan line stands for the correction assuming a realistic IFP curtain moving along the central meridian line as on Figure 7.8. The orange and the dashed green lines represent the correction assuming the same realistic curtain moving along the equator either toward dawn or toward dusk.

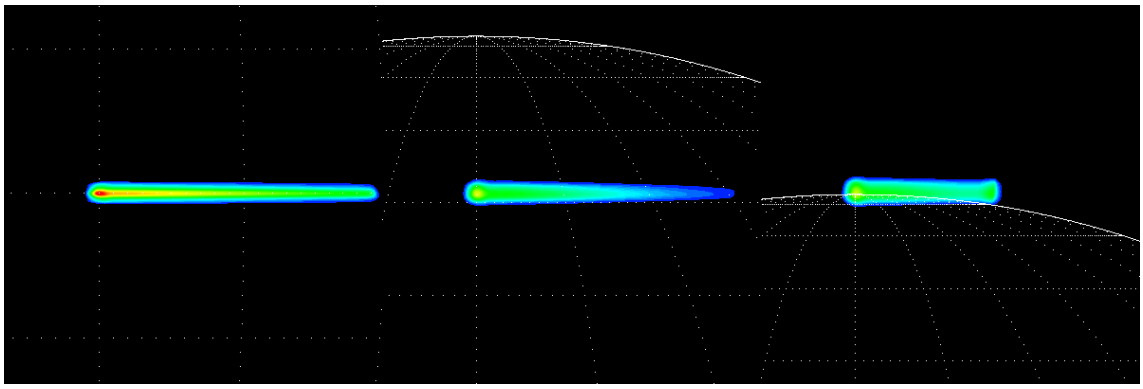

Figure 7.8: Evolution of the apparent brightness as a function of the latitude of the IFP (0°, 50° and 80°, respectively). The footprint is modeled as a single spot and an extended tail with a constant length. Because the IFP is a thin curtain with a large vertical extent, its apparent maximum brightness decreases when the spot approaches the limb along the central meridian. On the right side image, it is noticeable that the limb brightening effect induces an apparent brightness enhancement in the tail.

the nadir is 1 kR. Then we compute the best set of multiplicative coefficients (in the sense of the least squares) for the linear combination of the sub-images to reproduce the actual one.

All four sub-structures are aligned along the IFP reference contours described in Chapter 4. The relative position of the spots varies as a function of the System III longitude of Io as described in the same chapter. For spot "x", the vertically integrated brightness varies along and perpendicularly to the contour following a Gaussian law:

$$I_x(i,j) = e^{\left(-\frac{(i-lon_x)^2}{2\sigma^2_{lon_x}} - \frac{(j)^2}{2\sigma^2_{lat_x}}\right)}$$

where i is the distance along the contour, j is the distance perpendicular to the contour, lon_x is the position of the spot maximum along the contour as defined by the reference contour, σ_{lon_x} characterizes[3] the spot width along the contour, σ_{lat_x} characterizes the spot width perpendicularly to the contour.

As far as the tail is concerned, the perpendicular brightness profile is described by a Gaussian as well, but the evolution of the brightness along the contour is

[3]The relationship between the σ parameter of a Gaussian and its full width at half maximum ($FWHM$) is:

$$FWHM = 2.3548 * \sigma$$

	$FWHM_{lon}$ or e-folding distance	$FWHW_{lat}$	vertical scale height	peak altitude
MAW spot	900 km	200 km	400 km	900 km
TEB spot	900 km	200 km	200 km	700 km
RAW spot	900 km	200 km	400 km	900 km
Tail	20000 km	200 km	400 km	900 km

Table 7.2: Size parameters for the simulated spots and tail.

described by a function which starts as a polynomial law and then evolves as a decreasing exponential law. The form might look complex, but has been chosen because it allows to easily tune all the relevant parameters such as the position of the maximum and the e-folding distance:

$$I_{trail}(i,j) = a_t(i-d_{lon})^{n_t} e^{\left(-b_t*(i-d_{lon})-\frac{(j)^2}{2\sigma^2_{lat_t}}\right)}$$

with

$$a_t = \left(\frac{1}{lon_t}\right)^{n_t} e^{n_t}$$

$$b_t = \frac{n_t}{lon_t}$$

$$n_t = \frac{e^1}{\left(\frac{H}{lon_t}\right) - \ln\left(\frac{H}{lon_t}\right) - 1}$$

and where H is the e-folding distance, lon_t is the position of the tail maximum along the contour which is set to $lon_{MAW} + \sigma_{MAW}$ and d_{lon} is the tail starting position along the contour, which is set to $lon_{MAW} - \sigma_{MAW}$.

The brightness in the above equations corresponds to the vertically integrated brightness, which is the relevant parameter to derive the incoming particle flux. However, to compute the model images corresponding to an oblique observation, the vertical emission rate profile has to be specified and is described with a Chapman profile (see Equation 5.1). The parallel and perpendicular sizes of the different sub-structure as well as their altitude maximum and their vertical scale height are gathered in Table 7.2.

At this step of the process, we have defined the longitude, the latitude, the altitude and emission rates of the emission points corresponding to the different spots and the tail. The spatial coordinates are converted into x-y-z coordinates linked to

the HST image, x and y corresponding the image abscissae and ordinates and z corresponding to the depth. For each x-y couple, the emissions rates are summed along the z direction to produce the pixel brightness. One image is produced for each sub-structure and this image is subsequently convolved with the point spread function (PSF) corresponding to the relevant instrument and filter.

Because of the finite accuracy of the reference contour, the fine tuning of the simulated images position is computed by adjusting the barycenter of the MAW spot to the one of the disk emissions-free original image (see Chapter 2 for a description of the background planetary disk removal). The final step is a least squares fit of the relative brightnesses of the different IFP features to the original image. The fitting coefficients provide the maximum vertical brightness for each sub-structure in kR.

The two major limitations of this measurement method are 1) the impossibility to disentangle the MAW and the TEB spot when the Io centrifugal latitude is close to zero and 2) the description of the initial part of the tail. When the absolute value of the Io centrifugal latitude is below 2.5°, the TEB spot is no longer taken into account and the modeled MAW spot alone simulates the combination of the two spots. It is thus important to keep this fact in mind when interpreting the MAW brightness in these sectors. As far as the beginning of the tail is concerned, we chose a reasonable empirical formulation of the brightness along the contour because current models focus either on the initial phase of the interaction, leading to the spots, or on the tail when it is well established, but not specifically on the transition phase (Phase 2 in the *Delamere et al.* (2003) formulation).

7.4.4 Results and discussion

The method described above is not easy to implement and only preliminary results are available and presented here.

One of the main reasons to use brightness units instead of power units is the direct connection between the brightness as measured vertically from the emission point and the precipitating power. However, in the case of HST observation of the Jovian polar regions, the zenith angle is far from 0°. If the emission region is an extended area, the observed brightness can be easily converted into the vertical brightness by means of the parallel plane or the spherical shell approximations. Unfortunately, our measurements of the IFP size and shape demonstrated that the Io footprint is a thin curtain made of different spots and a tail and cannot be considered as an extended

area. Figure 7.7 showed that values computed with any correction method based on the extended area assumption are much smaller than the observed brightness, while a zenith observer would actually measure larger values than HST. Figure 7.9 shows the maximum brightness of the MAW spot as a function of the System III longitude of Io without any correction. The global trend seems to follow the previous conclusions from *Gérard et al.* (2006) and *Serio and Clarke* (2008). The maximum brightness is observed around 110°, and a possible second peak appears around 290° for the northern IFP, which corresponds to the region where Io is near the torus center. The main difference lies in the number of data points and in the brightness values, which are not reduced by any limb brightness correction.

Our new measurement method adresses a totally different point of view and tries to answer the question: What is the maximum vertical brightness that should be injected into the different spots and in the tail to reproduce the observations? The results for the MAW spot are shown in Figure 7.10.

First, we note that the plotted values are much larger than for earlier estimates (see Table 1.1). The first reason stems from the fact that the maximum brightness as observed from above is higher than seen from the side since the vertical scale height is assumed to be $\sim$ 400 km while the width is only $\sim$ 200 km wide. The second reason is related to the point spread function (PSF). In the above chapter related to the position and the size of the different features, we argued that the PSF has little effect because its FWHM is between one and two pixels. As far as the maximum brightness is concerned, the impact of the PSF cannot be neglected any more because a significant part of the energy is spread into the PSF wings.

Assuming that 10 kR seen looking at the nadir corresponds to an incoming electron energy flux of 1 mW/m^2, we find that the incoming flux for the MAW spot ranges between 100 and 500 mW/m^2. Consequently, the presence of such values raises once again the issue of the atmospheric response to such an sudden and concentrated energy supply.

Second, as for the non-corrected brightness, the behavior of the southern MAW spot vertical brightness shows two noticeable peaks around 110° and 290°. These sectors correspond to Io centrifugal latitudes around 0°, i.e. when Io is near the torus center. This result favors two possible scenarii: the one related to the strength of the interaction at Io and the one involving the merging of the spots.

Third, we note a huge brightness difference between the northern and the southern MAW spots in the longitude range between 150° and 200°. In this sector, Io is

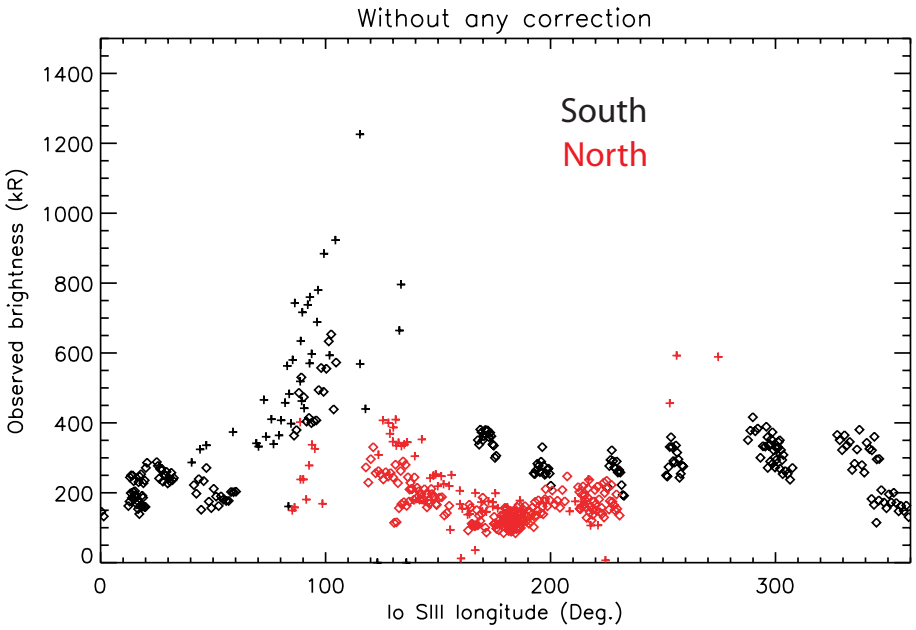

Figure 7.9: Evolution of the maximum observed brightness as a function of the Io longitude. Black symbols are for the southern hemisphere while red symbols are for the northern hemisphere. The "plus" symbols represent STIS observations while the "diamond" symbols represent ACS observations. No limb brightening correction was applied to the plotted values.

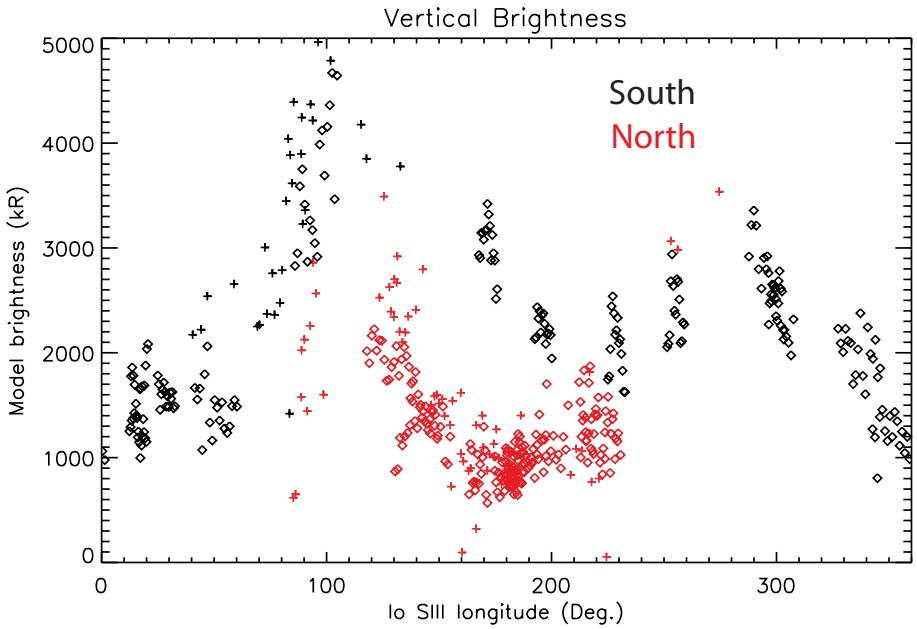

Figure 7.10: Evolution of the modeled maximum vertical brightness as a function of the Io longitude. Black symbols are for the southern hemisphere while red symbols are for the northern hemisphere. The "plus" symbols represent STIS observations while the "diamond" symbols represent ACS observations.

progressively moving from the torus center to the northern torus boundary. Figure 7.11 shows the emitted power as measured during two consecutive HST orbits. The telescope was pointing to the south pole during the first half of the orbit and then it is directed to the north. The northern spots are so faint that the MAW spot is fainter than the TEB spot in the south. The second orbit begins with North IFP observations and then the field of view shifts toward the South. This case is very interesting to test the different scenarii mentioned above because no long term variation of the torus density can be invoked to explain the observed differences. The different spots are well separated, so that their mixing cannot explain the spots brightness variations in this sector. On the other hand, if the strength of the interaction were the only driver for the spots brightness, then both hemispheres would have shown the same spots brightness. The Poynting flux loss hypothesis could not explain this difference either: since Io has positive centrifugal latitudes in this sector, the southward Alfvén wing crosses a longer distance in the torus than the northward wing. Consequently, the southern MAW spot should be weaker than the northern one, contrary to observations. The only remaining scenario that justifies

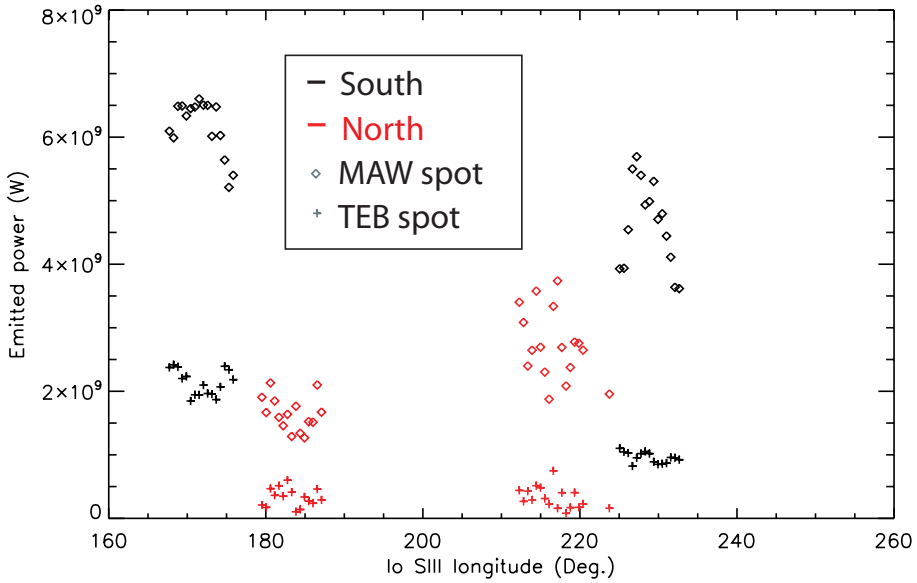

Figure 7.11: Evolution of the MAW spot ("diamond" symbols) and the TEB spot ("plus" symbols) emitted power during two consecutive orbits. The black symbols represent observations in the southern hemisphere and the red symbols represent observations in the northern hemisphere. The spot emissions are weaker in the North than in the South, which could be attributed to the difference of surface magnetic field strength.

the asymmetry between the hemispheres is the surface magnetic field. Indeed, the VIP4 magnetic field model predicts a weaker field strength in the south than in the north, facilitating electron precipitation. The influence of the surface magnetic field strength could also explain why the peak at 110° in the South is higher than at 290°. Similarly, it would also explain why the southern MAW spot is weaker around 10° than around 200°.

We have seen in the previous chapters that the different spots should be understood as individual features and we suggested that they might be caused by different mechanisms. It is thus necessary to analyze their behavior independently. Figure 7.12 shows the evolution of the MAW spot power and the TEB spot power for a southern IFP. In this range of longitudes, Io is coming from its southern most position and approaches the torus center. On the images, we can clearly see the spots progressively approaching each other. This case approximately corresponds to the case studied by *Serio and Clarke* (2008). They observed that the overall mean brightness increases whith time and they attributed this behavior to the enhancement of the interaction at Io. However, when we analyze the spots separately, only

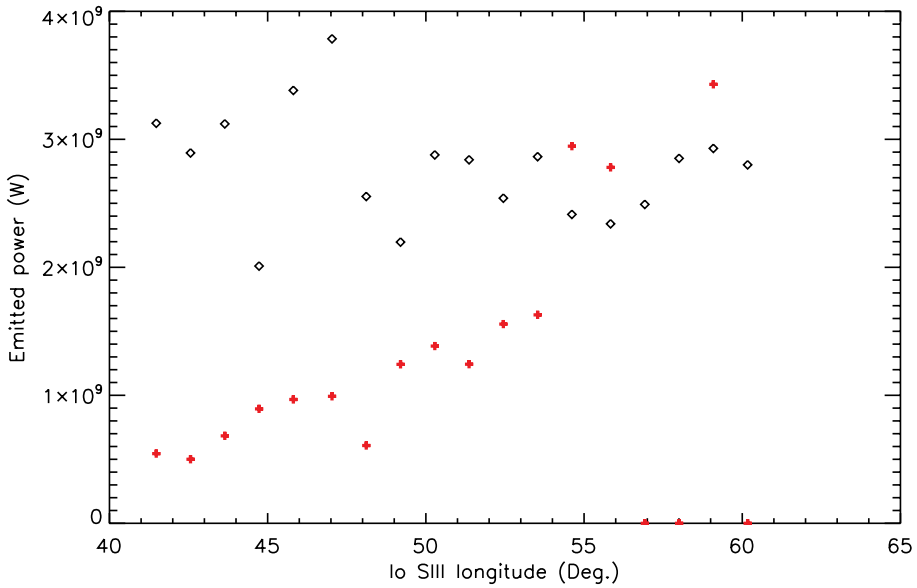

Figure 7.12: Evolution of the MAW spot (black "diamond" symbols) and the TEB spot (red "plus" symbols) emitted power during a single orbit in the southern hemisphere. As the TEB spot approaches the MAW spot, the power of the TEB spot increases while the power of the MAW spot remains roughly constant.

the TEB spot emitted power increases while the MAW spot power remains approximately constant. This observation thus challenges the previous interpretation of the brightness variations since, if the interaction at Io was driving the emitted power for both spots, both should be enhanced at the same time.

At this stage of our study, we must nevertheless be careful when interpreting the measurements. When Io's longitude is 60°, Io is not yet close to the torus center and the MAW spot brightness could still rise later because of the increasing interaction strength. The fact that the spots do not evolve in a correlated way on timescales on tens of minutes just confirms the idea that they originate from different processes. This finding does not necessarily contradict our previous finding of simultaneous fast variations of the same spots since the timescales are different.

7.5 Conclusions

The measurement of the Io footprint brightness requires a good understanding of the observing geometry. We use the spatial information gathered during the course of this work, such as the spots positions and the inter-spot distances as well as the

respective size and altitude of the different features, to develop a new method of analysis. This method consists in assessing how many times simulated spot images with well-known vertical brightness are necessary to best fit the original HST image. When possible, we try to distinguish the different spots. However, in sectors where the TEB and the MAW merge, i.e. when Io is close to the torus center, they cannot be disentangled. This could partly explain the apparent brightness enhancements of the MAW spot in these locations. Another scenario remains possible since the strength of the Io-magnetosphere increases in the dense torus center, which is also expected to lead to a brighter spot as well. When the spots are well separated, the MAW and the TEB spots can behave differently, one remaining constant while the other brightens with time. This finding seems to confirm one of the main results of this work: the different spots should be considered independently because they have different origins.

Another important result is the finding of an asymmetry of the northern brightness compared to the southern brightness. Added to the fact that the southern brightness at 110° is larger than at 290° while Io is at the same location in the torus, this information indicates that the surface magnetic field strength also plays a major role in the control of the spots brightness.

Moreover, the vertical brightness that we derive implies precipitating electron energy flux between 100 and 500 mW/m^2 for the MAW spot while previous estimates were lying closer to 30 mW/m^2.

Finally, we highlighted for the first time brightness variations on timescales of one minute. These variations reach up to 50% of the brightness with a typical growth time of 100 seconds. In some cases, the MAW and the TEB spot experience simultaneous variations over such short timescales, which suggests that the driving mechanism for the fast variations is located close to Jupiter. Brightness variations over similar timescales have later been found for the Ganymede footprint and in radio S-burst measurements. The latter also indicates that they could be related to an additional electron acceleration region located close to the planet. The idea that two acceleration mechanisms simultaneously contribute to the electron precipitation could also explain why correlated variations of the spots are seen on short timescales while a differentiated behavior is observed on longer timescales. The main electron acceleration mechanism would be related to the inertial Alfvén waves and would have a maximum efficiency around 1 R_j away from the planet (*Jones and Su*, 2008). Since the acceleration takes place relatively far from the planet, the surface magnetic field

strength could have an influence on the precipitated flux. Then, a second mechanism related to vertically migrating acceleration structures would appear at altitudes around $0.1R_j$. This interpretation would however require further observations and simulations to be fully confirmed.